Experimental Determination of the Topological Phase Diagram in Cerium Monopnictides

Kenta Kuroda,[1] M. Ochi,[2] H. S. Suzuki,[1,3] M. Hirayama,[4] M. Nakayama,[1] R. Noguchi,[1] C. Bareille,[1] S. Akebi,[1] S. Kunisada,[1] T. Muro,[5] M. D. Watson,[6] H. Kitazawa,[3] Y. Haga,[7] T. K. Kim,[6] M. Hoesch,[6] S. Shin,[1] R. Arita,[4] and Takeshi Kondo[1]

[1]*ISSP, University of Tokyo, Kashiwa, Chiba 277-8581, Japan*
[2]*Department of Physics, Osaka University, Machikaneyama-cho, Toyonaka, Osaka 560-0043, Japan*
[3]*National Institute for Materials Science, 1-2-1 Sengen, Tsukuba 305-0047, Japan*
[4]*RIKEN Center for Emergent Matter Science (CEMS), 2-1 Hirosawa, Wako, Saitama 351-0198, Japan*
[5]*Japan Synchrotron Radiation Research Institute (JASRI), 1-1-1 Kouto, Sayo, Hyogo 679-5198, Japan*
[6]*Diamond Light Source, Harwell Campus, Didcot OX11 0DE, United Kingdom*
[7]*Advanced Science Research Center, Japan Atomic Energy Agency, Tokai, Ibaraki 319-1195, Japan*

(Received 20 July 2017; revised manuscript received 9 January 2018; published 21 February 2018)

Experimental determinations of bulk band topology in the solid states have been so far restricted to only indirect investigation through the probing of surface states predicted by electronic structure calculations. We here present an alternative approach to determine the band topology by means of bulk-sensitive soft x-ray angle-resolved photoemission spectroscopy. We investigate the bulk electronic structures of the series materials, Ce monopnictides (CeP, CeAs, CeSb, and CeBi). By performing a paradigmatic study of the band structures as a function of their spin-orbit coupling, we draw the topological phase diagram and unambiguously reveal the topological phase transition from a trivial to a nontrivial regime in going from CeP to CeBi induced by the band inversion. The underlying mechanism of the phase transition is elucidated in terms of spin-orbit coupling in concert with their semimetallic band structures. Our comprehensive observations provide a new insight into the band topology hidden in the bulk states.

DOI: 10.1103/PhysRevLett.120.086402

The discovery of topological insulators represents a significant progress of topological band theory [1–3]. They are characterized by a nontrivial Z_2 topological invariant obtained if the conduction and valence bands with different parity are inverted due to spin-orbit coupling (SOC) [4]. In the three-dimensional case, the band inversion gives rise to topological surface states (TSSs) inside the energy gap. The concept was generalized to various systems, which has revealed the great richness of the intriguing topological phase [5–10].

Owing to the bulk-edge correspondence [11,12], investigations of the in-gap TSS in principle can indirectly reveal the band topology hidden in the bulk states. In fact, surface-sensitive angle-resolved photoemission spectroscopy (ARPES) with vacuum ultraviolet light (VUV) has achieved great success in confirming the Dirac-like TSS in a number of chalcogenides [13–17], which have obtained excellent agreement with the predicted nontrivial Z_2 topology [18–20].

However, searches of the topological phase are still challenging in low carrier semimetallic rare-earth monopnictides, with the NaCl-type crystal structure, LnX (Ln = La or Ce; X = P, As, Sb, or Bi) [21–28]. The main difficulty comes from two issues. One is that band calculation can show controversial conclusions about their band topology, since the magnitude of band gaps can be poorly estimated [21–23], and therefore the experimental determination is crucial. Secondly, despite this, so far the experimental confirmations are specialized for the observation of the surface dispersions predicted by the calculations [23–28], limiting one only to deduce the bulk band inversion. LaBi has been considered to be a topologically nontrivial state [24–27]. In LaSb, the Dirac-cone-like energy dispersion, has been observed and, however, the interpretation remains controversial [25,27,29]. Recent VUV ARPES showed the Dirac-cone-like dispersion also in CeSb and CeBi [28], but the interpretation is unclear. Thus there remains a necessity to directly determine the full bulk band structure and its topological character.

In this Letter, we present an alternative way to clarify the band topology by using bulk-sensitive soft x-ray (SX) ARPES in conjunction with theoretical parity analysis. For this demonstration, we adopt a series of materials of Ce monopnictides. By the paradigmatic investigation of their electronic structures from CeP to CeBi, we construct the topological phase diagram as a function of SOC. The obtained phase diagram unambiguously demonstrates the topological phase transition from a trivial to a nontrivial regime across the border between CeSb and CeBi.

Single crystalline CeX's were grown by using the Bridgman method. Bulk-sensitive SX-ARPES measurements were performed at BL25SU at SPring-8 [30]. The

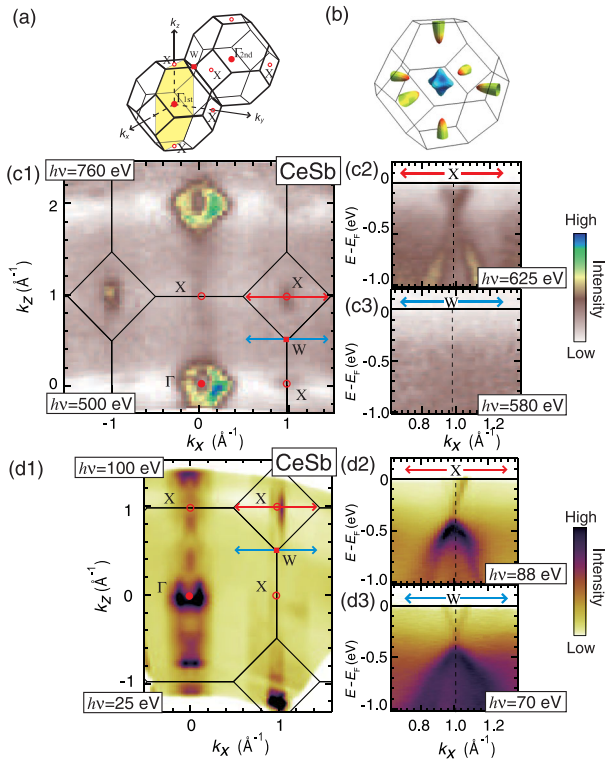

FIG. 1. (a) 3D Brillouin zone (BZ), showing the $k_z - k_x$ sheet at $k_y = 0$. (b) Calculated bulk Fermi surfaces (FSs). (c1) SX-ARPES result for FS mapping on the k_z-k_x plane [yellow plane in (a)] with different $h\nu$. (c2),(c3) SX-ARPES band maps cut along different k_x crossing X and W [red and blue lines in (c1), respectively]. (d1) VUV-ARPES FS mapping on the k_z-k_x plane by changing $h\nu$. (d2),(d3) VUV-ARPES band maps at different k_z as shown in (d1). The k_z value was obtained with the inner potential $V_0 = 12$ eV.

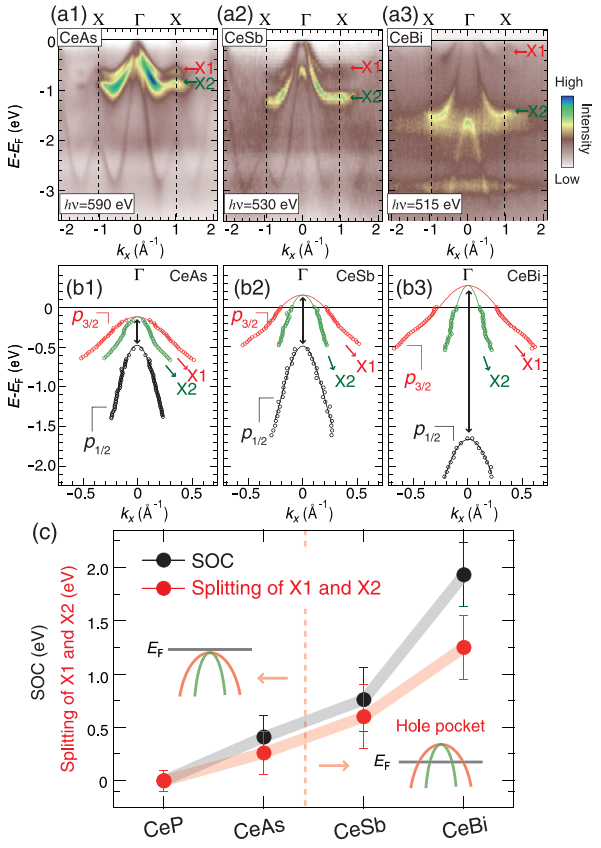

FIG. 2. (a1)–(a3) SX-ARPES band maps for CeX's cut along the X-Γ-X line obtained by the $h\nu$ of (CeAs) 590 eV, (CeSb) 530 eV, and (CeBi) 515 eV. (b1)–(b3) Comparison of (red and green) the $p_{3/2}$ and (black) $p_{1/2}$ energy dispersions around Γ. The energy dispersions are determined by tracing the peak position of the momentum distribution curves (MDCs). (c) Experimentally determined strength of their SOC. The size was defined as the energy difference for the top of $p_{3/2}$ and $p_{1/2}$ bands at Γ [black arrows in (b1)–(b3)]. The top of the bands is deduced by fitting analysis with quartic function (solid lines). The energy positions of $X1$ and $X2$ bands are obtained by the results presented in Fig. 3.

total experimental energy resolution was set to about 70–90 meV for photon energy ($h\nu$) of 500–760 eV. Surface-sensitive VUV-ARPES measurement was performed at I05 ARPES beam line at DIAMOND light source [31]. The total experimental energy resolution was set to below 20 meV for $h\nu$ of 25–100 eV. All samples were cleaved at a pressure of 5×10^{-8} Pa at approximately 60 K, exposing shiny surfaces corresponding to the (001) plane. The sample temperature was kept at 60 K during the measurement to avoid magnetic phases at low temperature [32–34].

We start with presenting bulk-sensitive SX-ARPES and surface-sensitive VUV-ARPES results for Fermi surface (FS) mappings in CeSb. Figure 1(c1) presents the FS mapping on the k_x-k_z plane [yellow plane in Fig. 1(a)] recorded with varying $h\nu$ from 500 to 760 eV. These data display the clear k_z dispersions and the FS topology of CeSb, which is consistent with calculation in Fig. 1(b), showing an elliptical electron pocket formed by Ce t_{2g} at X, and hole pockets originating from Sb $5p$ at Γ.

In contrast, the k_z dispersion is unclear in VUV ARPES [Fig. 1(d1)]. Figures 1(d2) and 1(d3) show the VUV-ARPES maps along different k_x cuts crossing X and W, respectively [red and blue lines in Fig. 1(d1)]. In both $h\nu$, we observe the Dirac-cone-like energy dispersion, which is seen even by using different $h\nu$ in the VUV range. This behavior is reminiscent of the surface state with no k_z dependence. Indeed, the Dirac-cone dispersion in CeSb was previously interpreted as the in-gap TSS [28]. However, we here come to an alternative conclusion. SX-ARPES measurements under a precise k_z definition [35] clearly observe the k_z dependence for the same band [Figs. 1(c1)–1(c3) and Note 2 [36]]. These facts identify the Dirac-cone-like dispersion as the 3D bulk states. Apparently, only with VUV ARPES, the determination of the bulk band topology in CeSb is very difficult. We therefore use SX ARPES to investigate the band topology of CeX's.

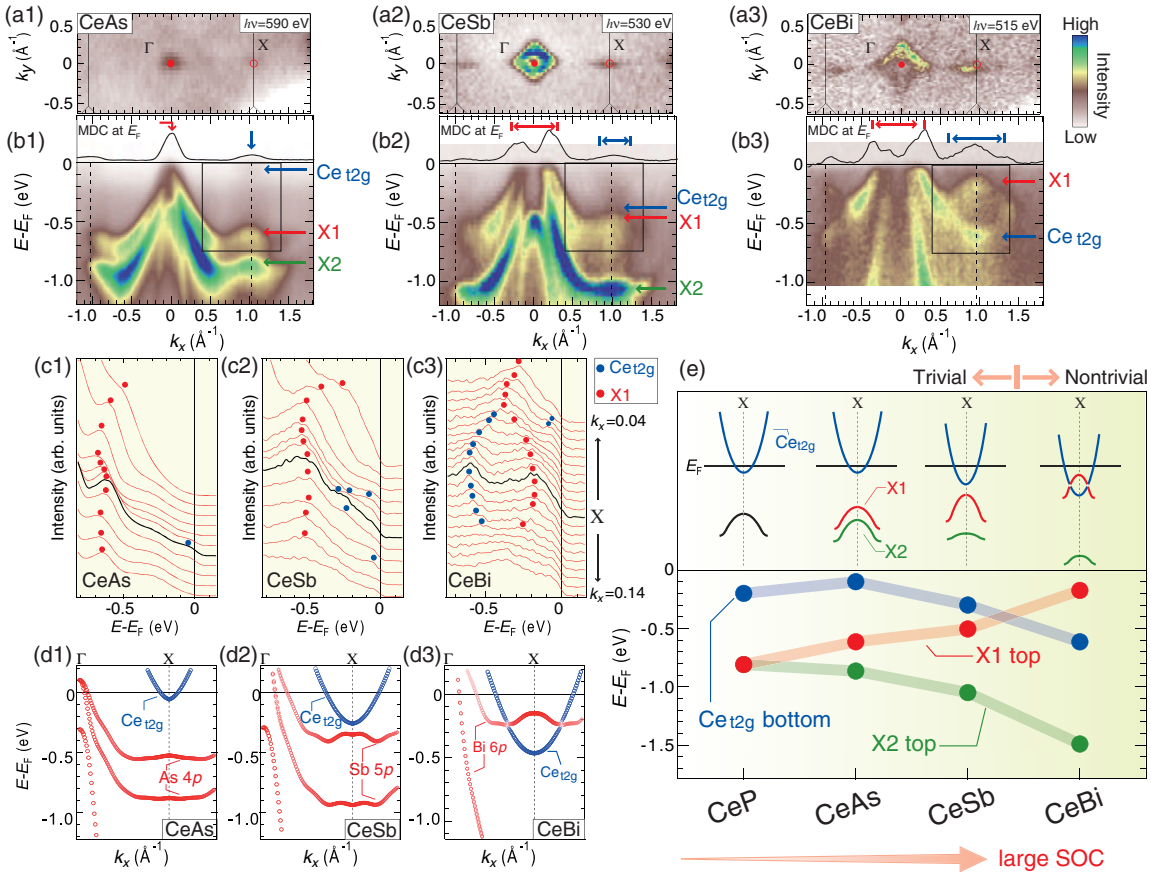

FIG. 3. (a1)–(a3) FS mapping on the k_x-k_y plane at $k_z = 0$ for CeX's. (b1)–(b3) Enlarged SX-ARPES band maps of Figs. 2(a1)–2(a3) and (inset) their MDCs at E_F. The hole (electron) pockets are shown by red (blue) arrows above the MDCs. (c1)–(c3) The energy distribution curves (EDCs) around X within the $E - k_x$ window in (b1)–(b3), displaying (red circles) $X1$ and (black circles) Ce t_{2g} dispersions. The EDC at X is highlighted by the black line. (d1)–(d3) The calculated band structures around X (Supplemental Material, Note 3 [36]). Red and blue represent the pnictogen p and Ce t_{2g} orbital contributions. For the calculation, we used the on-site-energy shift for Ce t_{2g}, $\Delta_{t2g} = 0.85$ eV (CeAs), 0.60 eV (CeSb), and 0.54 eV (CeBi). (e) Experimentally determined topological phase diagram with the energy positions of (blue) Ce t_{2g}, (red) $X1$, and (green) $X2$ bands (Table S1 [36]). (Inset) The schematics of the band structures around X.

We now turn to compare the bulk electronic structures of CeX's. By tuning $h\nu$ in the SX range, we selectively observe their bulk band dispersions in a wide energy range along X-Γ-X in Figs. 2(a1)–2(a3) (the data for CeP are presented in Fig. S1 [36]). By systematically looking at their electronic structures, we find the SOC effect and its evolution when moving in the pnictogen from P to Bi. In Figs. 2(b1)–2(b3), we show the detailed energy dispersions of the valence p bands around Γ, obtained by momentum distribution curves (MDCs). Because of the SOC, the p bands split into the $p_{1/2}$ and $p_{3/2}$ states. The magnitude of the splitting varies substantially across the series of compounds. Figure 2(c) represents the estimated size of their SOC (see the caption). In going from CeP to CeBi, the SOC strength becomes large from ∼0 eV up to ∼2 eV.

We find two important consequences of the SOC. First, the SOC induces the valence band splitting also at X [arrows in Figs. 2(a1)–2(a3)]. The large SOC pushes the $X1$ ($X2$) band up (down) in energy. The splitting becomes significant with increasing SOC [Fig. 2(c)]. Second, for CeSb and CeBi, the higher-lying $p_{3/2}$ bands are pushed above E_F due to the large SOC, and the hole pockets appear [Figs. 2(b2) and 2(b3)]. Since the CeX series materials have a similar low carrier density [37], the SOC evolution of the hole pockets should increase the size of the Ce t_{2g} electron pocket at X. This carrier compensation is necessary in the semimetallic structure of CeX.

The electron band evolution is captured in Figs. 3(a1)–3(a3) and 3(b1)–3(b3) where we present the FS mappings on the k_x-k_y plane at $k_z = 0$ and the enlarged band maps near E_F, respectively. The intensities from the Ce t_{2g} band are seen in the MDCs at E_F [insets of Figs. 3(b1)–3(b3)]. For CeAs, both the hole and electron pockets are quite small [Figs. 3(a1) and 3(b1)]. With growing the hole pocket at Γ from CeAs to CeBi [Figs. 3(b1)–3(b3)], the electron band bottom goes down in energy and the size of the electron pocket becomes large (blue arrows). In addition, one can trace $X1$ and $X2$ energy

TABLE I. The parity of three bands considered at eight time-reversal inversion momenta (TRIMs), Γ, 3X, and 4L (Supplemental Material, Note 3 [36]). The Z_2 index ν_0 can be expressed as the parity product over all TRIMs, $(-1)^{\nu_0} = \Pi_{i=0}^{8}\delta_i$, where δ_i is the parity product at each TRIM [4].

	CeP, CeAs, CeSb	CeBi
Γ	− − −	− + +
3X	− − −	− − +
4L	+ + +	+ + +
ν_0	0 (trivial)	1 (nontrivial)

dispersions in Figs. 3(b1)–3(b3). They disperse downwards in energy from Γ to X, and weakly upwards around X, as can be clearly seen in CeAs. The large splitting of $X1$ and $X2$ eventually leads to the band inversion in CeBi, which can be clearly seen in their EDCs around X, as shown in Figs. 3(c1)–3(c3). For CeAs, $X1$ (red circles) and Ce t_{2g} (blue circles) are separated in energy. In going from CeAs to CeBi, the holelike dispersion of $X1$ and the electronlike dispersion of Ce t_{2g} approach one another: CeSb forms the Dirac-cone-like energy dispersion with a small gap ∼0.1 eV, and these two bands are finally inverted in CeBi.

Figures 3(d1)–3(d3) show the calculated band structure with analyzing the orbital parity for CeX. The band gap obtained by SX-ARPES measurements is available to determine the realistic band topology. To do this, we introduce the on-site-energy shift for Ce t_{2g} orbitals in our tight-binding model (see the caption). The parity eigenvalues are specified for the p bands (red circles) and the Ce t_{2g} band (blue circles). The calculation of the Z_2 invariant of CeX is shown in Table I. The analysis indicates that only CeBi belongs to a topologically nontrivial phase due to the observed parity inversion at the X point. Other band inversions may occur at the unoccupied Γ point, similar to LaBi [26]. However, since the number of the band inversion at Γ is restricted in an even-numbered time, the resulting Z_2 invariant should be nontrivial for CeBi (Note 3 [36]).

Based on the SX-ARPES results and the parity analysis, one can now draw the topological phase diagram of CeX as shown in Fig. 3(e). The topological phase transition is elucidated by SOC in collaboration with the carrier compensation of the semimetallic structures. CeSb is trivial but close to a phase transition state while CeBi is classified into a nontrivial phase due to the band inversion. The band inversion process visualized by SX ARPES is the most fundamental feature of the topological matters, and therefore the presented nontrivial topology of CeBi is identified without surface information.

The overall bulk dispersions directly determined by SX ARPES now enable us to unravel the nontrivial surface states within the inverted band gap. To show this, we use standard VUV ARPES and study the surface dispersions on the cleaved (001) surface of CeBi [Fig. 4]. As reported in LaBi [21,26], we expect that the two surface states (SSs) emerge at $\bar{M}$ because the two X points in the bulk Brillouin zone are projected to an $\bar{M}$ in the surface Brillouin zone [Fig. 4(a)]. Our slab calculation presents two SSs within the inverted band gap [$s1$ and $s2$ shown in Fig. 4(d)], which is similar to those in LaBi [26,27]. As X and Γ are projected into $\bar{\Gamma}$, the odd number of the SSs should appear around $\bar{\Gamma}$. However, the calculated SS is fully buried inside the bulk continuum on the (001) surface, and thus unlikely detectable by ARPES.

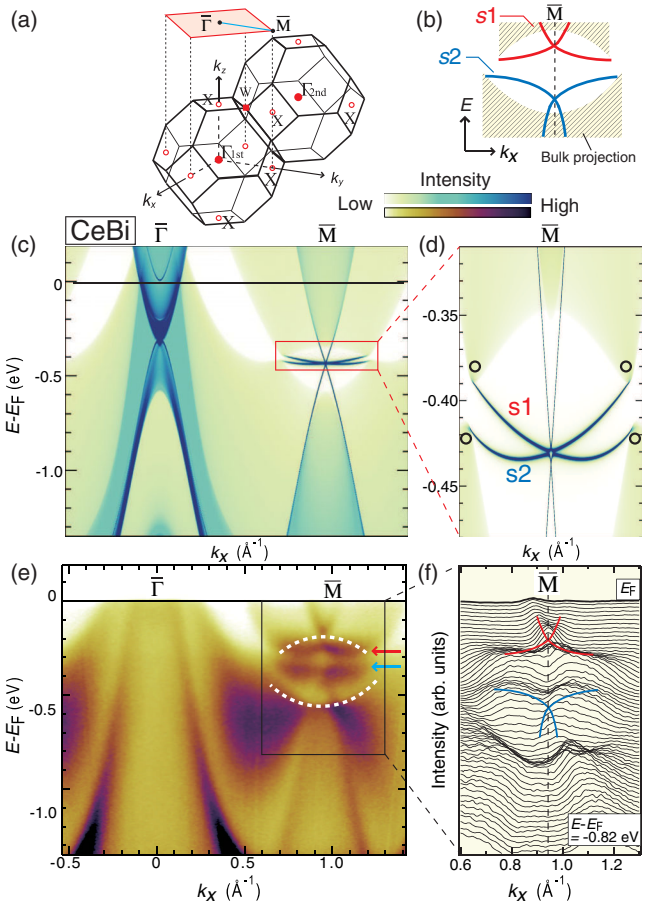

FIG. 4. (a) (001) surface BZ of CeBi. (b) Schematics of the observed surface dispersions induced by the parity inversion within the bulk projection gap. (c) Calculated (001) surface band structures along $\bar{\Gamma}$-$\bar{M}$ line [blue line in (a)]. For our semi-infinite slab calculations, two CeBi layers are regarded as a unit for the calculation scheme of the surface Green's function presented in Ref. [38], and so the surface spectral weight is defined for the top two CeBi layers. To fit our SX-ARPES data, E_F in the calculation results is shifted to be 0.10 eV. (d) Enlarged two surface states around $\bar{M}$ point. $s1$ and $s2$ label the surface bands (Note 5 [36]). (e) VUV-ARPES band map cut along $\bar{\Gamma}$-$\bar{M}$ with $h\nu = 55$ eV. The dashed lines guide the inverted bulk-band dispersions taken from Fig. 3(c3). The signals from $s1$ and $s2$ are indicated by arrows. (f) The MDCs around $\bar{M}$. The observed $s1$ and $s2$ are guided by colored lines.

In accordance with our slab calculation, we find the $s1$ and $s2$ bands around $\bar{M}$ in our VUV-ARPES results [Figs. 4(e) and 4(f)]. The intrinsic surface dispersion within the band gap can be disentangled from the irrelevant signals [marked by arrows in Fig. 4(e)]. The dispersions of the $s1$ and $s2$ bands are seen in the MDCs around $\bar{M}$ [Fig. 4(f)], which is illustrated also in Fig. 4(b). Within the band gap, $s1$ and $s2$ stay almost flat in energy at ~0.28 and ~0.35 eV, and both lose the spectral intensity with being close to the bulk continuum states. This overall shape of their dispersion shows good agreement with our slab calculation [Fig. 4(d) and Note 5 [36]].

In summary, we performed bulk-sensitive SX ARPES on CeX series materials and determined the topological phase diagram. Our experiment unambiguously demonstrated the topological transition from a trivial to a nontrivial phase across the border between CeSb and CeBi in the presented phase diagram. Moreover, the mechanism is explained by the SOC in concert with the carrier-compensated semimetallic band structures. This work proposes a new capability of SX ARPES to clarify the band topology, which can be widely applied for solid states as a complementary tool of surface-sensitive ARPES.

We thank Y. Yoshida for discussions and Y. Ishida for supporting analysis of ARPES data. We acknowledge support from Photon and Quantum Basic Research Coordinated Development Program from the Ministry of Education, Culture, Sports, Science and Technology, Japan. This work is also supported by Japan Science and Technology Agency, Grants-in-Aid for Scientific Research on Innovative Areas 'Topological Materials Science' (Grants No. 15H05852 and No. 16H00979), and Grants-in-Aid for Young Scientists A (Grant No. 16H06013) and B (Grant No. 17K14319). The SX synchrotron radiation experiments were performed with the approval of JASRI (Proposal No. 2017A1410). We thank Diamond Light Source for access to beamline I05 (SI16161-1) that contributed to the results presented here.

[1] M. Z. Hasan and C. L. Kane, Rev. Mod. Phys. **82**, 3045 (2010).
[2] X.-L. Qi and S.-C. Zhang, Rev. Mod. Phys. **83**, 1057 (2011).
[3] Y. Ando, J. Phys. Soc. Jpn. **82**, 102001 (2013).
[4] L. Fu and C. L. Kane, Phys. Rev. B **76**, 045302 (2007).
[5] S. Murakami, New J. Phys. **9**, 356 (2007).
[6] X. Wan, A. M. Turner, A. Vishwanath, and S. Y. Savrasov, Phys. Rev. B **83**, 205101 (2011).
[7] W. Witczak-Krempa, G. Chen, Y. B. Kim, and L. Balents, Annu. Rev. Condens. Matter Phys. **5**, 57 (2014).
[8] Y. Kim, B. J. Wieder, C. L. Kane, and A. M. Rappe, Phys. Rev. Lett. **115**, 036806 (2015).
[9] K. Mullen, B. Uchoa, and D. T. Glatzhofer, Phys. Rev. Lett. **115**, 026403 (2015).
[10] R. Yu, H. Weng, Z. Fang, X. Dai, and X. Hu, Phys. Rev. Lett. **115**, 036807 (2015).
[11] Y. Hatsugai, Phys. Rev. Lett. **71**, 3697 (1993).
[12] C. L. Kane and E. J. Mele, Phys. Rev. Lett. **95**, 146802 (2005).
[13] Y. Xia, D. Qian, D. Hsieh, L. Wray, A. Pal, H. Lin, A. Bansil, D. Grauer, Y. S. Hor, R. J. Cava *et al.*, Nat. Phys. **5**, 398 (2009).
[14] Y. Chen, J. Analytis, J.-H. Chu, Z. Liu, S.-K. Mo, X.-L. Qi, H. Zhang, D. Lu, X. Dai, Z. Fang *et al.*, Science **325**, 178 (2009).
[15] T. Sato, K. Segawa, H. Guo, K. Sugawara, S. Souma, T. Takahashi, and Y. Ando, Phys. Rev. Lett. **105**, 136802 (2010).
[16] K. Kuroda, M. Ye, A. Kimura, S. V. Eremeev, E. E. Krasovskii, E. V. Chulkov, Y. Ueda, K. Miyamoto, T. Okuda, K. Shimada, H. Namatame, and M. Taniguchi, Phys. Rev. Lett. **105**, 146801 (2010).
[17] Y. L. Chen, Z. K. Liu, J. G. Analytis, J.-H. Chu, H. J. Zhang, B. H. Yan, S.-K. Mo, R. G. Moore, D. H. Lu, I. R. Fisher, S. C. Zhang, Z. Hussain, and Z.-X. Shen, Phys. Rev. Lett. **105**, 266401 (2010).
[18] H. Zhang, C.-X. Liu, X.-L. Qi, X. Dai, Z. Fang, and S.-C. Zhang, Nat. Phys. **5**, 438 (2009).
[19] H. Lin, R. S. Markiewicz, L. A. Wray, L. Fu, M. Z. Hasan, and A. Bansil, Phys. Rev. Lett. **105**, 036404 (2010).
[20] B. Yan, C.-X. Liu, H.-J. Zhang, C.-Y. Yam, X.-L. Qi, T. Frauenheim, and S.-C. Zhang, Europhys. Lett. **90**, 37002 (2010).
[21] M. Zeng, C. Fang, G. Chang, Y.-A. Chen, T. Hsieh, A. Bansil, H. Lin, and L. Fu, arXiv:1504.03492.
[22] P.-J. Guo, H.-C. Yang, B.-J. Zhang, K. Liu, and Z.-Y. Lu, Phys. Rev. B **93**, 235142 (2016).
[23] L.-K. Zeng *et al.*, Phys. Rev. Lett. **117**, 127204 (2016).
[24] Y. Wu, T. Kong, L.-L. Wang, D. D. Johnson, D. Mou, L. Huang, B. Schrunk, S. L. Bud'ko, P. C. Canfield, and A. Kaminski, Phys. Rev. B **94**, 081108 (2016).
[25] X. H. Niu, D. F. Xu, Y. H. Bai, Q. Song, X. P. Shen, B. P. Xie, Z. Sun, Y. B. Huang, D. C. Peets, and D. L. Feng, Phys. Rev. B **94**, 165163 (2016).
[26] J. Nayak, S.-C. Wu, N. Kumar, C. Shekhar, S. Singh, J. Fink, E. E. Rienks, G. H. Fecher, S. S. Parkin, B. Yan *et al.*, Nat. Commun. **8**, 13942 (2017).
[27] R. Lou, B.-B. Fu, Q. N. Xu, P.-J. Guo, L.-Y. Kong, L.-K. Zeng, J.-Z. Ma, P. Richard, C. Fang, Y.-B. Huang, S.-S. Sun, Q. Wang, L. Wang, Y.-G. Shi, H. C. Lei, K. Liu, H. M. Weng, T. Qian, H. Ding, and S.-C. Wang, Phys. Rev. B **95**, 115140 (2017).
[28] N. Alidoust, A. Alexandradinata, S.-Y. Xu, I. Belopolski, S. K. Kushwaha, M. Zeng, M. Neupane, G. Bian, C. Liu, D. S. Sanchez *et al.*, arXiv:1604.08571.
[29] H. Oinuma, S. Souma, D. Takane, T. Nakamura, K. Nakayama, T. Mitsuhashi, K. Horiba, H. Kumigashira, M. Yoshida, A. Ochiai, T. Takahashi, and T. Sato, Phys. Rev. B **96**, 041120(R) (2017).
[30] Y. Senba, H. Ohashi, Y. Kotani, T. Nakamura, T. Muro, T. Ohkochi, N. Tsuji, H. Kishimoto, T. Miura, M. Tanaka *et al.*, AIP Conf. Proc. **1741**, 030044 (2016).

[31] M. Hoesch, T. Kim, P. Dudin, H. Wang, S. Scott, P. Harris, S. Patel, M. Matthews, D. Hawkins, S. Alcock *et al.*, Rev. Sci. Instrum. **88**, 013106 (2017).

[32] T. Kasuya, Y. Haga, Y. Kwon, and T. Suzuki, Physica (Amsterdam) **186B–188B**, 9 (1993).

[33] H. Kumigashira, H.-D. Kim, A. Ashihara, A. Chainani, T. Yokoya, T. Takahashi, A. Uesawa, and T. Suzuki, Phys. Rev. B **56**, 13654 (1997).

[34] H. Kumigashira, S.-H. Yang, T. Yokoya, A. Chainani, T. Takahashi, A. Uesawa, and T. Suzuki, Phys. Rev. B **55**, R3355 (1997).

[35] V. Strocov, J. Electron Spectrosc. Relat. Phenom. **130**, 65 (2003).

[36] See Supplemental Material at http://link.aps.org/supplemental/10.1103/PhysRevLett.120.086402 for additional SX-ARPES and VUV-ARPES data, and theoretical analysis of the band topoplogy.

[37] T. Suzuki, Physica (Amsterdam) **186B–188B**, 347 (1993).

[38] M. P. L. Sancho, J. M. L. Sancho, J. M. L. Sancho, and J. Rubio, J. Phys. F **15**, 851 (1985).